Buoyant convection from a discrete source in a leaky porous medium

By MARK A. ROES[1], DIOGO T. BOLSTER[2], AND M. R. FLYNN[1]†

[1]Department of Mechanical Engineering, University of Alberta, Edmonton, AB T6G 2G8 Canada

[2]Department of Civil & Environmental Engineering & Earth Sciences, University of Notre Dame, Notre Dame, IN 46556

(Received 8 October 2015)

The application of turbulent plume theory in describing the dynamics of emptying filling boxes, control volumes connected to an infinite exterior through a series of openings along the upper and lower boundaries, has yielded novel strategies for the natural ventilation of buildings. Making the plume laminar and having it fall through a porous medium yields a problem of fundamental significance in its own right, insights from which may be applied e.g. in minimizing the contamination of drinking water by geologically-sequestered CO_2 or the chemicals leached from waste piles. After reviewing the theory appropriate to rectilinear and axisymmetric plumes in porous media, we demonstrate how the model equations may be adapted to the case of an emptying filling box. In this circumstance, the long-time solution consists of two ambient layers, each of which has a uniform density. The lower and upper layers are comprised of fluid that is respectively discharged by the plume and advected into the box through the upper opening. Our theory provides an estimate for both the height and thickness of the associated interface in terms of e.g. the source volume and buoyancy fluxes, the outlet area and permeability and the depth-

† Corresponding author email: mrflynn@ualberta.ca

average solute dispersion coefficient, which is itself a function of the far-field horizontal flow speed. Complementary laboratory experiments are provided for the case of a line source plume and show very good agreement with model predictions. Our measurements also indicate that the permeability, k_f, of the lower opening (or fissure) decreases with the density of the fluid being discharged, a fact that has been overlooked in some previous studies wherein k_f is assumed to depend only on the fissure geometry.

---

1. Introduction

The study of density-driven flow from a point or line source of positive or negative buoyancy has received much attention since the seminal work of Morton, Taylor & Turner (1956, hereafter referred to as MTT), who derived an analytical model describing turbulent plumes. They developed and closed conservation of mass, momentum and buoyancy equations for the plumes by proposing a simple yet robust expression for lateral entrainment. Specifically MTT assumed that the entrainment velocity is directly proportional to a characteristic vertical rise velocity within the plume. The MTT equations have been demonstrated as useful in studying manifold topics including models of fires (Drysdale 2011), volcanic eruptions (Woods 1988), bubble (McDougall 1978, Wüest, Brooks & Imboden 1992) and hydrothermal plumes (Speer & Rona 1989), oil leakage from the deep ocean (Adalsteinsson et al. 2011) as well as various other natural flows (Woods 2010). For the sake of simplicity, here we will only discuss a negatively-buoyant plume with flow downwards, although all points are equally relevant to positively-buoyant upwards moving plumes.

By adapting MTT, Baines & Turner (1969) considered the situation where the turbulent plume flows in an enclosed space, giving rise to the so-called *filling box model*. In this

flow, the turbulent plume falls and results, by mass conservation, in a background return flow in the opposite upwards direction. Assuming that the cross-sectional area occupied by the plume is much less than the total cross-sectional area of the domain, Baines & Turner (1969) showed that the timescales of the plume and of the background return flow can be decoupled leading to a problem that can be analyzed theoretically in a systematic manner. Baines & Turner's description has been used across a number of disciplines to study, for example, deep ocean (Killworth 1983, Wong & Griffiths 2001) and magma chamber convection (Turner & Campbell 1986), smoke dynamics during fires in enclosed spaces (Kaye & Hunt 2007) and overturning in industrial storage tanks (Germeles 1975).

Later, it was recognized that if the same *box* had openings along the lower and upper boundary that connect to an infinite external ambient fluid, a natural flow arises due to differences in the internal and external hydrostatic pressure distributions (Linden, Lane-Serff & Smeed 1990). This flow leads to the ventilation of the box and is correspondingly termed the *emptying filling box*. The system evolves in such a way that a steady state is attained whereby the box is partitioned into two regions of different density, divided by a horizontal interface. The upper region is the area into which the external fluid flows in; its density matches that of the ambient. The lower region has a larger density, which equals that of the plume at the elevation of the interface. One of the most interesting aspects of the emptying filling box is that the interface height is independent of the source buoyancy flux and only depends on the size of the upper and lower openings and the box height. Thus if the source buoyancy flux changes, the flow naturally adjusts along with the rate of inflow and outflow in such a way that the previous interface height is restored, albeit after some transient. Emptying filling box models have enjoyed significant success and have been broadly applied to describe the natural ventilation of single enclosed spaces (Linden 1999). More generally, they have been adapted to study

the ventilation of adjacent building zones (Flynn & Caulfield 2006, Nabi & Flynn 2014), transient ventilation dynamics (Bower et al. 2008) and interior contaminant transport (Bolster & Linden 2007).

As indicated by the above list of references, the bulk of effort to date in this field has been to study high Reynolds number turbulent flows. However, there exist similar problems of interest in the field of environmental fluid mechanics that arise at much smaller length-scales and Reynolds numbers, namely convective flow through porous media. Here the mechanism for plume widening is fundamentally different than in the turbulent case: widening is driven not by engulfment via turbulent eddies but rather molecular or mechanical dispersion. From a purely conceptual perspective, however, many other dynamical features hold true. Studying emptying filling box models in porous media should therefore give rise to qualitatively similar, though quantitatively different, behaviors from what has been documented by Linden et al. (1990) and others. Of course, the literature describing buoyancy-driven convection in porous media is itself vast. Many models have been developed that include, among other effects, inertia, viscous dissipation and rotation – see e.g. Nield & Kuznetsov (2013) and the many references therein. Importantly, however, much of this literature assumes a distributed source with comparatively less attention devoted to the discrete source problem. This represents a nontrivial omission because discrete sources of buoyancy are commonplace in a broad number of environmental scenarios. These include, for instance, (i) dissolution of dense/light non-aqueous phase fluids (DNAPL/LNAPL) into potable groundwater, which have been shown to be one of the most persistent and dangerous forms of contamination in groundwater systems (National Research Council 2012), (ii) leakage of geologically-sequestered CO_2 from deep saline aquifers into higher, potentially potable, water aquifers (Nordbotten, Celia & Bachu 2004, Neufeld et al. 2011), and, (iii) leakage of contaminants from waste piles

(Kuo & Ritchie 1999) or composting facilities (Barrington et al. 2003). In each of these systems, engineered or naturally-occurring geologic barriers, with imperfections through which leakage will occur, can exist to confine the flow giving rise to the emptying filling box scenario. While realistic geometries might be quite complicated, we begin by focusing on an idealized rectangular enclosure from which much valuable information can be gleaned.

In this paper we present the equivalent MTT plume and emptying filling box models for flow in a porous medium. In §2 we develop the theory for a line source for both an open and an emptying filling box system. The equivalent model for an axisymmetric source representing a discrete point source is outlined in §3. Thereafter in §4 we describe complementary laboratory experiments designed to corroborate the predictions of §2. Qualitative and quantitative comparisons between theory and experiment are presented in §5. Finally §6 discusses conclusions of this work and identifies possible avenues for future investigations.

2. Theory – line source

We begin by considering the motion of a negatively-buoyant line plume, of buoyancy flux F_0, in an unbounded porous medium. The coordinate axes are oriented as in figure 1 a, which indicates that the plume originates from an infinitesimally thin source. The flow is assumed to be Boussinesq so that density differences may be omitted except where they multiply gravitational acceleration. We further assume that the Rayleigh number (defined by equation 2.15 below) is large and that the flow is Darcian (non-Darcy effects may be included through the introduction of Dupuit-Forchheimer terms – see Lai 1991 or, for a more general treatment, Joseph, Nield & Papanicolaou 1982). Accordingly, the

governing equations read (Turcotte & Schubert 2014)

$$\frac{\partial u}{\partial x} + \frac{\partial v}{\partial y} = 0\,, \tag{2.1}$$

$$\frac{1}{\rho_0}\frac{\partial P}{\partial x} + \frac{\nu}{k}u = \frac{g\rho}{\rho_0}\,, \tag{2.2}$$

$$\frac{1}{\rho_0}\frac{\partial P}{\partial y} + \frac{\nu}{k}v = 0\,, \tag{2.3}$$

$$\frac{1}{\phi}\left(u\frac{\partial S}{\partial x} + v\frac{\partial S}{\partial y}\right) = D\left(\frac{\partial^2 S}{\partial x^2} + \frac{\partial^2 S}{\partial y^2}\right)\,, \tag{2.4}$$

$$\rho = \rho_0(1 + \beta S)\,. \tag{2.5}$$

Here P is the fluid pressure, $\mathbf{u} = (u, v)$ is the transport velocity, ϕ is the void fraction, ν is the kinematic viscosity, S is the solute concentration, β is the solute contraction coefficient, k is the permeability and D is a solute dispersion coefficient, which is assumed not to vary with x or y and is described in more detail below. Moreover, ρ is the fluid density; when, as in the far-field, the fluid does not contain any solute, $\rho = \rho_0$. Finally, in evaluating the permeability, we use the Rumpf & Gupte (1971) relationship such that

$$k = \frac{1}{5.6}\bar{d}^2\phi^{5.5}\,,$$

where $\bar{d}$ denotes the mean diameter of the solid particles comprising the porous medium – see also (3.2) of Acton et al. (2001). When the particle diameter is uniform, we replace $\bar{d}$ with d.

Following the discussion of Wooding (1963), Phillips (1991) and Turcotte & Schubert (2014), self-similar solutions to (2.1-2.5) are sought that respect the following conditions:

$$\left|\frac{\partial u}{\partial y}\right| \gg \left|\frac{\partial v}{\partial x}\right|, \qquad \text{and} \qquad \left|\frac{\partial^2 S}{\partial y^2}\right| \gg \left|\frac{\partial^2 S}{\partial x^2}\right|. \tag{2.6}$$

Physically, these assumptions constitute a boundary layer approximation; when the plume is long and thin, changes of a dependent variable in the longitudinal direction will, in general, be much larger than changes in the lateral direction. After some algebra,

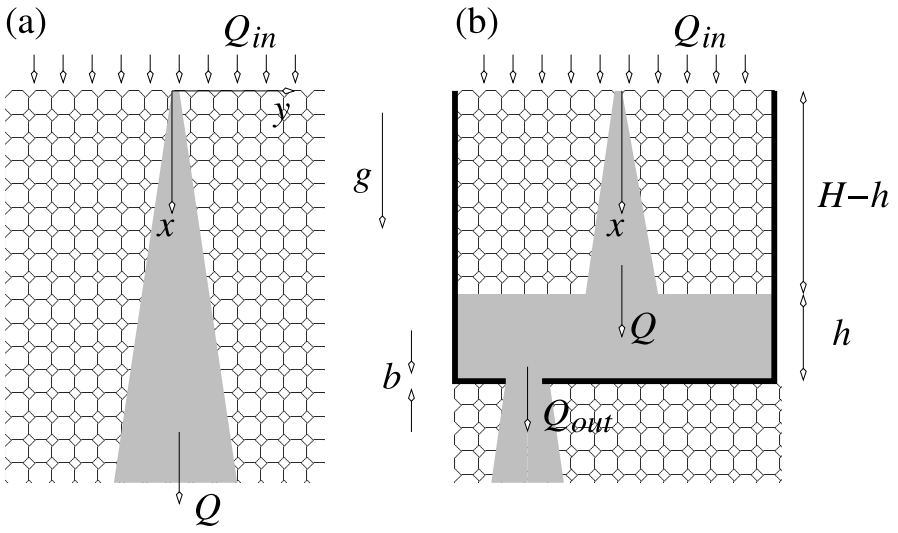

FIGURE 1. (a) Schematic of a two-dimensional Cartesian plume falling through an unbounded porous medium. (b) An emptying filling box containing a negatively-buoyant plume in a "leaky" porous medium. The control volume height and width are H and W, respectively, where the control volume refers to the region enclosed by the thick solid lines.

it can be shown that the plume momentum and volume fluxes respectively satisfy

$$M = \frac{F_0 k}{\nu}\,, \tag{2.7}$$

and

$$Q = \left(\frac{36 D\phi F_0 k x \Lambda^2}{\nu}\right)^{1/3}\,, \tag{2.8}$$

where Λ is the depth the line source extends into the page. (The latter equation is derived in Appendix A). Thus the plume volume flux increases with depth as $x^{1/3}$, which yields a corresponding dilution of plume fluid; defining $\bar{g'} \equiv F_0/Q$ as the average reduced gravity of the plume fluid at a particular elevation we find that

$$\bar{g'} = \left(\frac{F_0^2 \nu}{36 D\phi k x \Lambda^2}\right)^{1/3}\,. \tag{2.9}$$

The parameter D that appears in the previous equations represents a hydrodynamic

dispersion coefficient and is therefore the sum of two contributions, one molecular and the other mechanical. Following the discussion of Freeze & Cherry (1979) and Fetter (1993), we write

$$D = \alpha \bar{U} + \omega D_{\text{molecular}} \,, \tag{2.10}$$

where α is the dynamic dispersivity, $\bar{U}$ is a characteristic speed, $D_{\text{molecular}}$ is the molecular diffusion transport coefficient and $\omega\,(<1)$ is a parameter that depends on the tortuosity, i.e. the shape of the flow-path. For the flow depicted schematically in figure 1, $\alpha\bar{U}$ is assumed to be much larger than $\omega D_{\text{molecular}}$ so that $D \simeq \alpha\bar{U}$. Implicit in this result is the fact that it is the transverse, rather than the longitudinal, component of the dispersion that is of interest (Houseworth 1984). Although this transverse component is often related to a speed in the longitudinal direction, for a flow such as that studied here, which is characterized by inflow and plume widening, we find it more appropriate to set $\bar{U}$ equal to the depth-average far-field horizontal speed. In principle D can vary with x and y due to spatial variations of velocity (Lai 1991), however our aim is to define a representative constant value over the domain of interest. The justification for this approach plus an explicit formula for D will be provided later; first we must define the vertical expanse over which this depth-average speed is to be computed.

The previous analysis makes only indirect reference to lateral boundaries, however, it is of interest to examine the draining flow that develops when the negatively-buoyant plume is placed inside a fixed control volume, say of height H and width W. As shown in figure 1 b, we consider a ventilated (or "leaky") control volume so that solute-bearing fluid may slowly drain through one or more discrete fissure(s) that appear along the bottom boundary of the control volume.

In this preliminary investigation, attention is restricted to steady conditions whereby $\mathrm{d}h/\mathrm{d}t = 0$ in which h is defined as in figure 1 b. When $\mathrm{d}h/\mathrm{d}t = 0$, the volume fluxes Q_{in},

$Q|_{H-h}$ and $Q_{\rm out}$ must be equal where the latter is given by

$$Q_{\rm out} = \frac{Ak_f \bar{g'}|_{H-h}}{\nu}\left(\frac{h+b}{b}\right) \tag{2.11}$$

(c.f. equation 2.1 of Neufeld, Vella & Huppert 2009 – see also Pritchard & Hogg 2002). Here k_f and b denote, respectively, the fissure permeability and depth. Conversely A denotes the fissure cross-sectional area. Finally $\bar{g'}|_{H-h}$ is determined from (2.9), i.e.

$$\bar{g'}|_{H-h} = \left[\frac{F_0^2\nu}{36D\phi k(H-h)\Lambda^2}\right]^{1/3}. \tag{2.12}$$

Equating $Q|_{H-h}$ from (2.8) with $Q_{\rm out}$ from (2.11) indicates that

$$\left[\frac{36D\phi F_0 k(H-h)\Lambda^2}{\nu}\right]^{1/3} = \frac{Ak_f}{\nu}\left(\frac{h+b}{b}\right)\left[\frac{F_0^2\nu}{36D\phi k(H-h)\Lambda^2}\right]^{1/3} \tag{2.13}$$

Rearranging this result yields a cubic polynomial equation that must be solved for the interface height $h = \xi H$, i.e.

$$\begin{aligned} 0 = {} & \left(\frac{A}{\Lambda b}\right)^3\left(\frac{k_f}{k}\right)^3\xi^3 + \left[\frac{3b}{H}\left(\frac{A}{\Lambda b}\right)^3\left(\frac{k_f}{k}\right)^3 - \frac{1}{\rm Ra}\right]\xi^2 \\ & + \left[3\left(\frac{b}{H}\right)^2\left(\frac{A}{\Lambda b}\right)^3\left(\frac{k_f}{k}\right)^3 + \frac{2}{\rm Ra}\right]\xi + \left(\frac{b}{H}\right)^3\left(\frac{A}{\Lambda b}\right)^3\left(\frac{k_f}{k}\right)^3 - \frac{1}{\rm Ra}, \end{aligned} \tag{2.14}$$

where the Rayleigh number, $\mathrm{Ra}\,(\gg 1)$, is defined by

$$\mathrm{Ra} = \frac{F_0 kH}{(36D\phi)^2\Lambda\nu} \tag{2.15}$$

(c.f. Phillips 1991, equation 7.5.25). Note that, consistent with the related analysis of Linden et al. (1990) for high Reynolds number single-phase fluid flow, the steady interface height is predicted to be independent of the width, W, of the filling box. Important differences from Linden et al. (1990) are identified below.

The above equations, and indeed the similarity solutions of (A 4), presume an ideal source with vanishingly small volume flux at the origin, $x = 0$. When this assumption cannot be justified, (2.8) must be modified by writing

$$Q = \left[\frac{36D\phi F_0 k(x+x_0)\Lambda^2}{\nu}\right]^{1/3}, \tag{2.16}$$

where x_0 is a virtual origin correction (Wooding 1963), defined as

$$x_0 = \frac{Q_0^3 \nu}{36 D \phi F_0 k \Lambda^2}\,. \tag{2.17}$$

Here $Q_0\,(>0)$ is the source volume flux. In like fashion, the density of the lower layer is determined via

$$\bar{g'}|_{H-h} = \left[\frac{F_0^2 \nu}{36 D \phi k (H-h+x_0)\Lambda^2}\right]^{1/3}. \tag{2.18}$$

Thus the interface height is estimated not from (2.14) but rather

$$\begin{aligned} 0 = &\left(\frac{A}{\Lambda b}\right)^3 \left(\frac{k_f}{k}\right)^3 \xi^3 + \left[\frac{3b}{H}\left(\frac{A}{\Lambda b}\right)^3 \left(\frac{k_f}{k}\right)^3 - \frac{1}{\mathrm{Ra}}\right]\xi^2 \\ &+ \left[3\left(\frac{b}{H}\right)^2 \left(\frac{A}{\Lambda b}\right)^3 \left(\frac{k_f}{k}\right)^3 + \frac{2}{\mathrm{Ra}}\left(1+\frac{x_0}{H}\right)\right]\xi \\ &+ \left(\frac{b}{H}\right)^3 \left(\frac{A}{\Lambda b}\right)^3 \left(\frac{k_f}{k}\right)^3 - \frac{1}{\mathrm{Ra}}\left(1+\frac{x_0}{H}\right)^2. \end{aligned} \tag{2.19}$$

Because ξ must, on physical grounds, lie between 0 and 1, at least one of the terms from (2.19) must be a negative number. We therefore require

$$\frac{3b}{H}\left(\frac{A}{\Lambda b}\right)^3 \left(\frac{k_f}{k}\right)^3 < \frac{1}{\mathrm{Ra}}\,, \tag{2.20}$$

and/or

$$\left(\frac{b}{H}\right)^3 \left(\frac{A}{\Lambda b}\right)^3 \left(\frac{k_f}{k}\right)^3 < \frac{1}{\mathrm{Ra}}\left(1+\frac{x_0}{H}\right)^2. \tag{2.21}$$

By definition $x_0 \geq 0$ and b/H is typically less or much less than unity; we therefore expect (2.21) to be satisfied before (2.20). In instances where neither inequality is satisfied, $\xi = 0$, i.e. there is no accumulation of solute-bearing fluid along the bottom boundary because the draining flow can more than accommodate all of the fluid discharged by the plume.

Solutions to (2.19) are given in figure 2, which shows the variation of ξ with $A/(\Lambda b)$ and Ra for various k_f/k, b/H and x_0/H. In all four cases, ξ is predicted to decrease with Ra and the non-dimensional cross-sectional area of the fissure, $A/(\Lambda b)$. Physically, as source buoyancy effects become more significant, the interface height decreases because

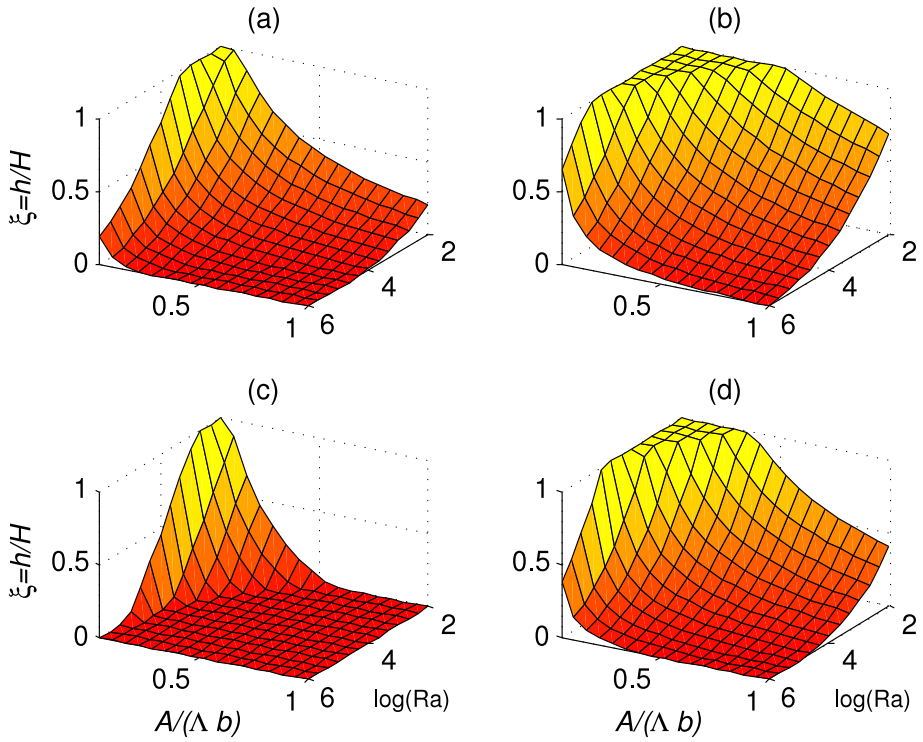

FIGURE 2. [color online] Non-dimensional lower layer depth, $\xi = h/H$, vs. $A/(\Lambda b)$ and Ra as determined from the solution of (2.19). (a) $k_f/k = 1$, $b/H = 0.05$, $x_0/H = 0.5$; (b) $k_f/k = 0.25$, $b/H = 0.05$, $x_0/H = 0.5$; (c) $k_f/k = 1$, $b/H = 0.5$, $x_0/H = 0.5$; and (d) $k_f/k = 1$, $b/H = 0.05$, $x_0/H = 2.5$. Note that $\min[A/(\Lambda b)] = 0.05$, not 0.

of an increase in the natural ventilation rate, which allows the system to flush more quickly. This is fundamentally different from the investigation of Linden et al. (1990) where viscous effects are ignored so that $\mathrm{Ra} \to \infty$. Similarly as the outlet area increases (relative, say, to some measure of the flow resistance provided by the fissure), the system can ventilate more efficiently resulting in smaller values for ξ. This finding is consistent with the study of Linden et al. (1990).

In figure 2 b, we imagine a scenario in which the fissure shape is modified leading to a fourfold decrease in the fissure permeability, k_f. There is therefore a greater resistance to flow through the fissure resulting in larger values for ξ. Conversely, in panel c, b/H

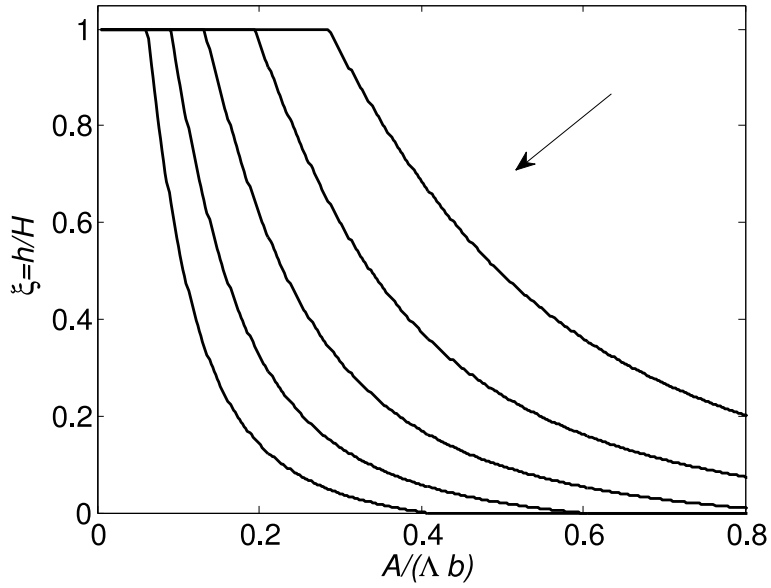

FIGURE 3. Non-dimensional lower layer depth, $\xi = h/H$, vs. $A/(\Lambda b)$ for Ra $= 10^2$, $10^3 \ldots 10^6$ (the arrow indicates the direction of increasing Ra). Here $b/H = 0.05$, $x_0/H = 0.5$ and k_f/k is determined using (2.22) with $\phi = 0.4$ and $A = \pi d_f^2/4$.

is increased from 0.05 to 0.5; the corresponding increase of hydrostatic pressure yields larger values for Q_{out} and smaller values for ξ. Finally, panel d considers an increase in the source volume flux, i.e. an increase in x_0, defined by (2.17). As a result of this extra volume of solute-bearing fluid supplied to the reservoir, ξ is larger than in the small x_0 case.

A limitation of the preceding analysis is that it implicitly assumes that the fissure area and permeability are independent variables, when in fact k_f can depend strongly on A. For the case of well-developed flow through a circular fissure of diameter d_f, for example, Bear (1972) equation (5.10.3) states that

$$k_f = \phi \frac{d_f^2}{32} \,. \tag{2.22}$$

Figure 3 confirms that qualitatively similar results are obtained when $k_f = k_f(A)$.

The preceding analysis also provides a means of predicting the thickness, $2L$, of the

ambient interface that develops between the layer of diluted solute-bearing fluid and the overlying layer of fresh ambient fluid. As summarized by Baines (1983), $2L$ is dictated by a balance between dispersion and lateral inflow into the plume, which tend to broaden and contract the interface, respectively. Presuming a one-dimensional problem, the time rate of increase of the interfacial volume by broadening is expressed as

$$(\Delta Q)_{\text{dispersion}} = \frac{4W\Lambda D}{L} \tag{2.23}$$

(c.f. equation 2.4 of Kaye et al. 2010). Conversely, (2.8) indicates that $Q \sim x^{1/3}$; therefore, the plume will have a moderately larger volume flux at the lower boundary of the thick interface (at $x = H - h + L$) as compared to at the upper boundary (at $x = H - h - L$). The difference of plume volume fluxes can be estimated from

$$(\Delta Q)_{\text{inflow}} = \left(\frac{36D\phi F_0 k\Lambda^2}{\nu}\right)^{1/3} \left[(H-h+L+x_0)^{1/3} - (H-h-L+x_0)^{1/3}\right] . \tag{2.24}$$

Equating the expressions from (2.23) and (2.24) yields

$$\frac{W}{9\phi H} = \ell\,\mathrm{Ra}^{1/3}\left[\left(1-\xi+\ell+\frac{x_0}{H}\right)^{1/3} - \left(1-\xi-\ell+\frac{x_0}{H}\right)^{1/3}\right] , \tag{2.25}$$

where $\ell \equiv L/H$.

Figure 4 shows ℓ as a function of $A/(\Lambda b)$ and Ra for the same parameter combinations as in figure 2. Results are shown only where ξ, defined by the physical root of (2.19), is neither 0 or 1. Thus ℓ is observed to be an increasing function of the fissure area, permeability and source volume flux and a decreasing function of Ra.

Equation (2.25) admits two asymptotic limits of interest, namely $(1-\xi+x_0/H) \gg \ell$ and $(1-\xi+x_0/H) \ll \ell$, in which case the interface is respectively thin and thick relative to the lower layer depth. In the former circumstance, (2.25) indicates that

$$\ell \sim \frac{1}{\mathrm{Ra}^{1/6}}\left(1-\xi+\frac{x_0}{H}\right)^{1/3}\sqrt{\frac{W}{6\phi H}} . \tag{2.26}$$

Note that ℓ scales with W, the reservoir width, as $\ell \sim \sqrt{W}$ and with the Rayleigh number

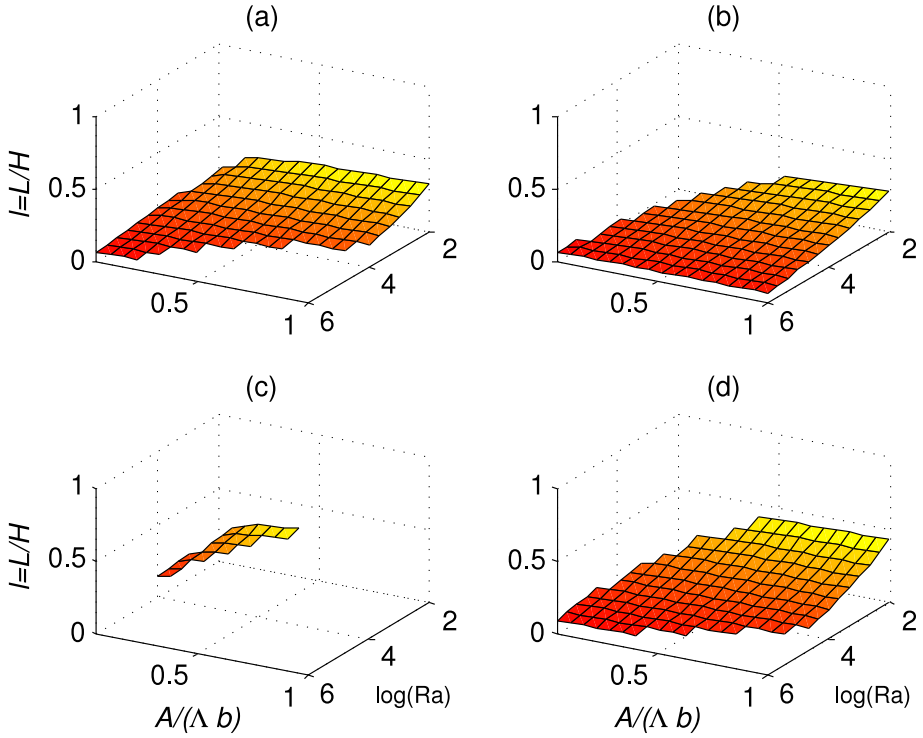

FIGURE 4. [color online] Non-dimensional half-thickness of the thick interface, $\ell = L/H$, vs. $A/(\Lambda b)$ and Ra as determined from the solution of (2.25). Parameter values are the same as in figure 2. Also $W/H = 1$ and $\phi = 0.4$.

as $\ell \sim \mathrm{Ra}^{-1/6}$. Moreover, ℓ increases, albeit relatively slowly, with $1 - \xi$, the vertical distance between the source and the interface. Interestingly, precisely the opposite trend is noted in the turbulent plume case studied by Baines (1983) and Kaye et al. (2010). Using the present notation, (2.7) of Kaye et al. (2010) indicates that $\ell \sim (1 - \xi)^{-1/3}$. Because $1 - \xi$ increases with the fissure area, this difference is reflected also in the fact that ℓ is an increasing function of $A/(\Lambda b)$ according to figure 4 whereas figure 2 of Kaye et al. (2010) shows that ℓ decreases as the area for outflow is increased. The reason for this difference of behavior is ultimately related to the variation of the plume volume flux with the vertical coordinate. When $Q \propto x^n$ and $n < 1$ ($n > 1$), ℓ will be a increasing (decreasing) function of $1-\xi$ and A. The ostensibly trivial case $n = 1$ in fact corresponds

to the opposite asymptotic limit for which $(1-\xi+x_0/H) \ll \ell$. Here

$$\ell \sim \frac{1}{\mathrm{Ra}^{1/4}} \left(\frac{W}{18\phi H}\right)^{3/4} . \tag{2.27}$$

The interface thickness is then independent of ξ and also the source volume flux i.e. x_0/H though still dependent on Ra. A comparable result applies also for turbulent plumes – see (2.8) of Kaye et al. (2010).

Implicit in the above calculations is the fact that, in the absence of plume inflow, ℓ varies as $\sqrt{Dt}$ where t is time. This result allows us to estimate the approximate timescale, t_{ss}, over which the interface reaches its steady state thickness, which may be quite long, particularly if the box width is large in some suitable non-dimensional measure. Normalizing t_{ss} by H^2/D, it can be shown that

$$\tau \equiv \frac{t_{ss}}{H^2/D} = \frac{1}{\mathrm{Ra}^{1/3}} \left(1-\xi+\frac{x_0}{H}\right)^{2/3} \frac{W}{24\phi H} , \tag{2.28}$$

and

$$\tau \equiv \frac{t_{ss}}{H^2/D} = \frac{1}{108\sqrt{\mathrm{Ra}}} \left(\frac{W}{2\phi H}\right)^{3/2} , \tag{2.29}$$

for the asymptotic limits given by (2.26) and (2.27), respectively.

Finally, it is necessary to return to the evaluation of D, which appears only vicariously in figures 2, 3 and 4. As noted following (2.10), we select as the characteristic speed the depth-average far-field value for v. Employing (A 13), this average speed is given by

$$|v_{ff,\mathrm{avg}}| = \frac{1}{3} \left(\frac{9D\phi F_0 k}{2\Lambda\nu}\right)^{1/3} \times \frac{1}{H} \int_{x_0}^{H+x_0} \frac{1}{x^{2/3}} \,\mathrm{d}x , \tag{2.30}$$

where the subscript *ff* indicates the far-field. Further applying (2.17) yields, after some straightforward algebra, the following nonlinear equation to be solved for the solute dispersion coefficient:

$$D^{2/3} = \frac{d}{H} \left(\frac{9\phi F_0 k}{2\Lambda\nu}\right)^{1/3} \left[\left(H + \frac{Q_0^3\nu}{36D\phi F_0 k\Lambda^2}\right)^{1/3} - \left(\frac{Q_0^3\nu}{36D\phi F_0 k\Lambda^2}\right)^{1/3}\right] . \tag{2.31}$$

Consistent with many analyses of porous media flow (e.g. Wooding 1963, Riaz et al. 2006,

Szulczewski et al. 2013, Turcotte & Schubert 2014), we assume a constant value for the dispersion coefficient, D. Doing so allows us to exploit the self-similar solutions presented in Appendices A and B and draws attention to the average effect of dispersion while ignoring its spatial variability. By contrast the far-field horizontal flow speed, whose depth-average value appears in (2.30), decreases by a factor of $(1 + H/x_0)^{2/3}$ between $x = x_0$ and $x = H+x_0$. Note, however, that the vertical variation of v_{ff} is most significant for small x/H. This is also the region where the boundary layer approximation is most suspect. If the top 20% of the control volume is ignored, v_{ff} decreases by less than a factor of 3, suggesting that the variation in D is also relatively modest. As we will reinforce in §5, the assumption $D =$ constant therefore provides sufficient physics to capture the details of the bulk flow.

3. Theory – axisymmetric source

The results of §2 can be readily extended to the case of a (negatively-buoyant) axisymmetric plume issuing from a point source. From the analysis of Appendix B, we find that the plume volume flux is in this case given by

$$Q = 8\pi D\phi x\,. \tag{3.1}$$

In contrast to (2.8), Q varies linearly with x and does not depend on the permeability or kinematic viscosity. The volume flux is also independent of the buoyancy flux: when the plume fluid is very dense, the plume will fall rapidly and remain relatively thin as compared to a less dense plume that falls more slowly (Turcotte & Schubert 2014). Because Q depends on both the vertical velocity and the cross-sectional area of the plume, there is a balance between competing effects that renders the volume flux insensitive to the magnitude of F_0, provided of course that the source buoyancy flux is large enough for high-Ra number convection to be established in the first place.

Whereas (3.1) describes an ideal plume such that $Q \to 0$ as $x \to 0$, it is again helpful to consider a non-ideal plume with finite source volume flux, $Q_0 > 0$. Thus (3.1) is replaced with

$$Q = 8\pi D\phi(x + x_0)\,, \qquad \text{where} \qquad x_0 = \frac{Q_0}{8\pi D\phi}\,. \tag{3.2}$$

Using (3.2) it is straightforward to derive the analogue of (2.9), which reads

$$\bar{g'} = \frac{F_0}{8\pi D\phi(x + x_0)}\,. \tag{3.3}$$

By extension,

$$\bar{g'}|_{H-h} = \frac{F_0}{8\pi D\phi(H - h + x_0)}\,. \tag{3.4}$$

When (2.11) and (3.2) are combined, the following (implicit) expression for the non-dimensional interface thickness, ξ, is obtained:

$$0 = \frac{1}{\mathrm{Ra}}\xi^2 - \left[\frac{b}{H}\left(\frac{k_f}{k}\right)\left(\frac{A}{b^2}\right) + \frac{2}{\mathrm{Ra}}\left(1 + \frac{x_0}{H}\right)\right]\xi - \left(\frac{b}{H}\right)^2\left(\frac{k_f}{k}\right)\left(\frac{A}{b^2}\right) + \frac{1}{\mathrm{Ra}}\left(1 + \frac{x_0}{H}\right)^2\,. \tag{3.5}$$

Here the Rayleigh number is now defined as

$$\mathrm{Ra} = \frac{F_0 k}{(8\pi D\phi)^2\nu}\,. \tag{3.6}$$

As compared to the right-hand side of (2.19), that of (3.5) is a quadratic, not a cubic, polynomial. Note, moreover, that each term from (3.5) is proportional to k^{-1}. Consequently, and in contrast to the data of figure 2, ξ is not expected to vary with the permeability of the reservoir.

Solutions of (3.5) are presented in figure 5 where, consistent with figure 2, we consider two different values for each of k_f/k, b/H and x_0/H. The variation of ξ with these parameters is qualitatively similar to that observed in the line source case. Thus figure 5 shows that ξ is a decreasing function of Ra and the non-dimensional fissure area, which is here denoted by A/b^2.

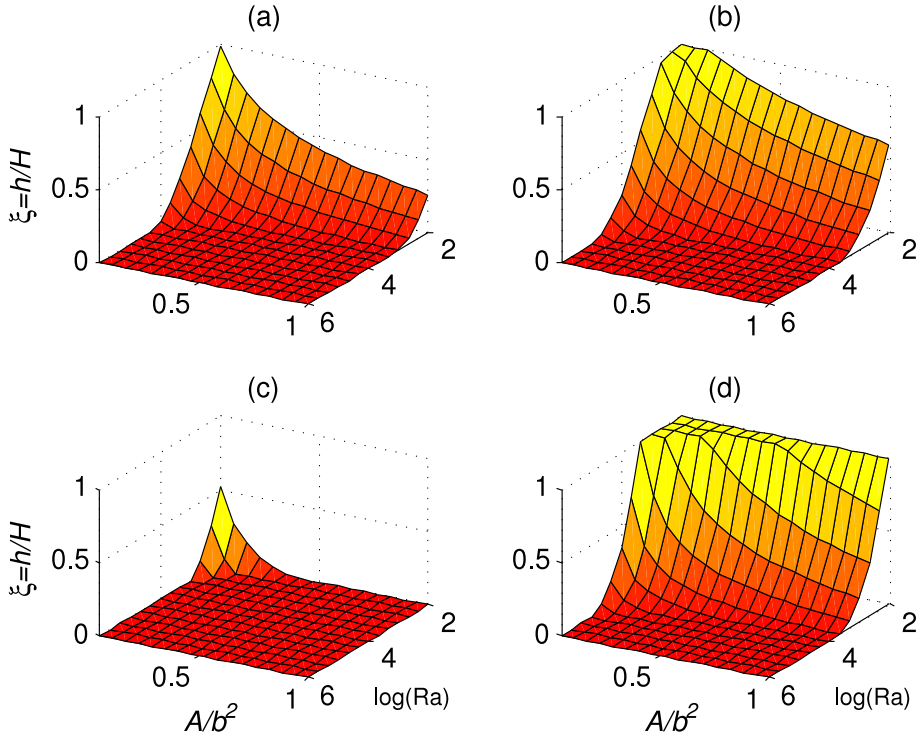

FIGURE 5. [color online] Non-dimensional lower layer depth, $\xi = h/H$, vs. A/b^2 and Ra as determined from the solution of (3.5). (a) $k_f/k = 1$, $b/H = 0.05$, $x_0/H = 0.5$; (b) $k_f/k = 0.25$, $b/H = 0.05$, $x_0/H = 0.5$; (c) $k_f/k = 1$, $b/H = 0.25$, $x_0/H = 0.5$; and (d) $k_f/k = 1$, $b/H = 0.05$, $x_0/H = 2.5$. Note that $\min[A/(\Lambda b)] = 0.05$, not 0.

We turn finally to the evaluation of the interface thickness, $2L$ and find a result that is qualitatively quite different from (2.25). Because the plume volume flux varies linearly with x,

$$(\Delta Q)_{\text{inflow}} = 16\pi D\phi L\,. \tag{3.7}$$

Conversely,

$$(\Delta Q)_{\text{dispersion}} = \frac{4A_r D}{L}\,, \tag{3.8}$$

where A_r is the reservoir cross-sectional area. Equating these expressions yields

$$\ell = \frac{1}{2H}\sqrt{\frac{A_r}{\pi\phi}}\,. \tag{3.9}$$

As expected from our discussion of (2.26), ℓ does not depend on any of the virtual origin correction, the distance from the source to the interface or the fissure area. The interface thickness is moreover independent of the buoyancy flux and the solute dispersion coefficient. The former observation stems from the fact that Q likewise does not vary with F_0. The latter stems from the fact that by increasing D, both the plume volume flux and the rate of interfacial broadening also increase. In fact, because D appears as a linear term in both (3.7) and (3.8), these competing effects exactly balance one another.

When the reservoir cross-section is rectangular and circular, respectively, (3.9) may be further simplified as follows

$$\ell_{\text{rectangular}} = \frac{1}{2H}\sqrt{\frac{W\Lambda}{\pi\phi}}\,, \qquad \ell_{\text{circular}} = \frac{R}{2H\sqrt{\phi}}\,. \tag{3.10}$$

These results reinforce the fact that ℓ now depends only on the void fraction and reservoir geometry. Note finally that the respective times required for the thick interface to spread to the values prescribed by (3.10) are approximated by

$$\tau_{\text{rectangular}} = \frac{W}{16\pi\phi H}\,, \qquad \tau_{\text{circular}} = \frac{1}{16\phi}\left(\frac{R}{H}\right)^2\,. \tag{3.11}$$

4. Laboratory experiments

Verification of the above predictions by laboratory experiment proved nontrivial. In the point source case, it was difficult to reconcile the large volume of porous medium required with the small source volume flux. Solute- i.e. NaCl-bearing fluid was found to become diluted so readily with fresh ambient fluid that one could not estimate h with adequate confidence. Consequently, the present discussion is restricted to the case of a rectilinear source, mimicking the discussion of §2.

Experiments were conducted in a clear acrylic box with internal dimensions 7.6 cm deep $\times$ 32.5 cm wide $\times$ 40.6 cm tall (figure 6). This box was filled to a depth of approximately

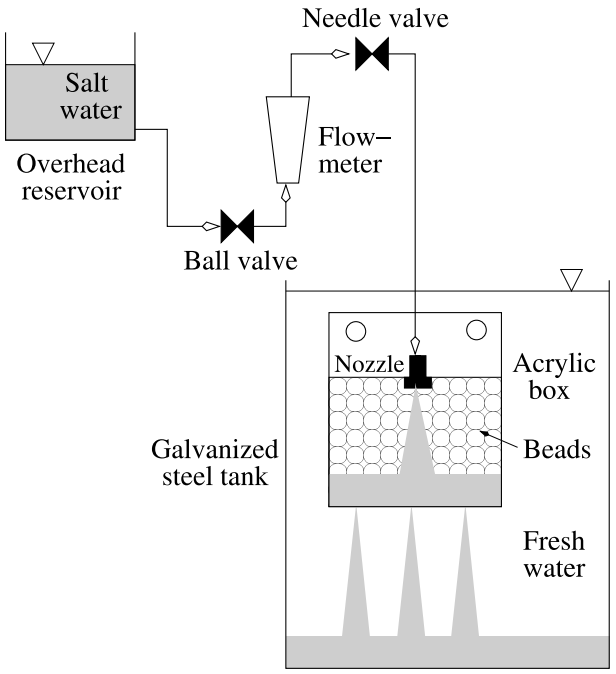

FIGURE 6. Experimental schematic showing the direction of flow from the overhead reservoir to the descending plume inside the acrylic box.

33.5 cm with Potters Industries A Series Premium glass beads, which had a nominal diameter of 3 mm. In the analysis to follow, we assume that $\phi = 0.4$ (Happel & Brenner 1991). To assist in measuring interface heights, a ruler was affixed to one side of the tank using double-sided adhesive tape. The bottom boundary of the acrylic box contained eight equidistant vents, each 2.54 cm in diameter, into which solid or one-hole stoppers could be inserted. A similar array of vents was located along the top of the front and back sides of the acrylic box; hole centers were positioned 3.81 cm apart, 2.54 cm from the top edge and approximately 3-4 cm above the bead interface. Finally, a hole of diameter 2.22 cm was drilled through the center of the top plate. Through this hole flowed dyed saline fluid inside of plastic tubing and a vertical copper conduit sleeve. The saline fluid was discharged through a nozzle, which we describe below.

Saline fluid was dyed with Procion MX Cold Water dye and was supplied from a 65 L overhead plastic reservoir. In the prototypical experiment, this fluid flowed, in sequence, through a ball valve, flowmeter and needle valve. The latter was used to set the plume source volume flux, whose value was $Q_0 = 0.1\,\mathrm{mL/s}$. Although a constant level was not maintained in the plastic reservoir, the free surface fell very slowly owing to the small outflux and relatively large cross-sectional area of the reservoir (59 cm × 42 cm). For long experiments, the needle valve was progressively opened by hand to maintain a constant value for Q_0.

Once inside the acrylic box, the saline fluid was discharged through a specially-built line source nozzle that spanned the box depth and which was located a vertical distance of approximately 1.5 cm below the bead interface. As described by Roes (2014), the internal structure of the nozzle was designed so that the flow remained relatively uniform along its length, even for small rates of discharge. The nozzle slit was 0.4 cm in width and was flared so as to reduce the importance of momentum as saline fluid flowed into the porous medium. Although the slit width is comparable to the bead diameter, (i) the plume radius will be shown to increase nontrivially with x (see e.g. figure 8 a below), and, (ii) it was impractical to run experiments having a smaller bead diameter because this would very substantially curtail the widening of the plume.

The acrylic box was suspended inside a much larger galvanized steel tank, whose volumetric capacity was approximately $2.2\,\mathrm{m}^3$. The steel tank had a square cross-section and stood approximately 1.81 m tall; for ease of flow visualization, each tank face contained a viewing window measuring 0.55 m by 1.80 m. Mimicking the flow described by the label Q_{in} in figure 1 b, fresh water from the tank flowed into the acrylic box through four of the 2.54 cm diameter vents located at the top of the box. Conversely, dense fluid drained through a series of much smaller openings along the bottom of the box. There was thus

a continual exchange between the fluid inside the acrylic box and that inside the steel tank. Note that in order to observe nontrivial values for h, the fissure cross-sectional area, A, had to be smaller even than the cross-sectional area associated with standard one-hole stoppers. As such, a series of eight acrylonitrile butadiene styrene (ABS) plastic inserts were manufactured using a Object Eden350V 3D printer. The inserts were fit inside existing one hole stoppers and had a length and inner diameter of $b = 2.0\,\mathrm{cm}$ and $d_f = 0.14\,\mathrm{cm}$, respectively. As many as eight and as few as two inserts were used during a given experiment. Any vents that did not contain a stopper fitted with an insert were instead plugged with a solid stopper, which did not admit any outflow of dense fluid.

Before running an experiment, the steel tank was filled to capacity with tap water and left to sit overnight. The water inside the tank therefore reached thermal equilibrium with the surrounding air. Concurrently, the acrylic box was suspended inside the steel tank so that its top surface sat approximately 5 cm below the eventual free surface. Special precautions were taken to minimize the volume of air that became trapped inside the pore space of the acrylic box (Roes 2014).

Two types of experimental runs were conducted. In the former, termed "draining flow" experiments, the descending plume of figure 1 was absent. Rather, the acrylic box was filled from the bottom and with negligible mixing with dyed saline fluid of prescribed density. All the while, this same fluid drained from the bottom of the acrylic box. Although there were eight open inserts through which dense fluid drained, the rate of filling exceeded the rate of draining. The interface therefore rose as a function of time, t. Once it reached a height of approximately 31 cm, the ball valve was closed ceasing the inlet flow. The time rate of descent of the interface was then recorded by collecting regularly-spaced digital images of the acrylic box and its contents. For this purpose, we used a Canon Rebel EOS T2i 18.0 megapixel camera with an 18-55 mm IS II zoom lens. To

minimize parallax effects, the camera lens was positioned 90 cm in front of the steel tank; backlighting using an overhead projector was applied for purposes of illumination. From the experimental data so collected, we could estimate k_f as a function of the density of the fluid flowing through the fissure – see figure 7 below.

The more prototypical experiment was of emptying filling box variety. Here, the initial condition again consisted of a porous medium saturated with fresh water. Now, however, the acrylic box was filled from the top and so produced a descending plume (figure 1). Upon reaching the bottom of the box, discharged plume fluid spread laterally then collected in an expanding layer. The terminal height of this dense lower layer was dictated by the balance between the fluid supplied by the plume and that discharged from the bottom of the box through the inserts, which numbered two, three, four, six or eight. Three values for the density of the source fluid were considered, namely $\rho_s = 1.0114\,\mathrm{g/cm^3}$, $1.0402\,\mathrm{g/cm^3}$ and $1.0700\,\mathrm{g/cm^3}$. These corresponded to respective $\bar{g'}_0$ values of $12.5\,\mathrm{cm/s^2}$, $42.0\,\mathrm{cm/s^2}$ and $71.5\,\mathrm{cm/s^2}$ where $\bar{g'}_0 \equiv \bar{g'}(x=0)$ is the reduced gravity of the fluid in the plastic reservoir. In all cases, and also with the draining flow experiments described previously, densities were measured using an Anton Paar DMA 38 densitometer. This device was accurate to $\pm 0.00005\,\mathrm{g/cm^3}$. Experiments were typically run in sequence where the fissure cross-sectional area, A, was progressively decreased. After changing the bottom boundary condition e.g. by replacing two of the stoppers containing inserts with two solid stoppers, approximately 45 minutes was required in order for a new steady state, consisting of a deeper lower layer, to be realized. At this point, images were recorded using the same optical set-up as described above.

Whether considering draining flow or emptying filling box experiments, estimates for h were derived from laboratory images using the same three-step post-processing algorithm (Roes 2014). Images were first resized and cropped so as to remove both regions outside

of the acrylic box and, if appropriate, the center region occupied by the descending plume. Next, the initial reference state was subtracted from each image in a particular experimental run. Changes to the depth of the dyed lower layer were therefore highlighted and a false-color image was produced. An initial estimate for the interface height, $\hat{h}$, was obtained by binning pixels into 10×10 boxes, computing the row-wise average of the boxes then determining the elevation where the change of intensity achieved a maximum value. To improve upon this estimate, we focused more specifically on those data that fell within ±150 pixel units of the the pixel assigned to $\hat{h}$, a vertical span of approximately 13-14 cm. Row-by-row, intensity values were again averaged and a polynomial curve was fit through the resulting data. After calculating the vertical derivative of this curve, we assigned our experimental estimate for h based on the extremum of the derivative (Kaye & Hunt 2004). Results were verified by overlaying the experimental estimate for h on top of the appropriate laboratory image; excellent agreement was noted in all cases.

5. Results and discussion

5.1. *Experimental determination of k_f/ϕ*

Appendix C presents a means by which measured data from the draining flow experiments may be used to estimate the value of k_f/ϕ. On this basis, we found that k_f/ϕ is a decreasing function of the fluid density, approaching the well-developed flow prediction of $d_f^2/32$ only for sufficiently large $\bar{g}'$ (figure 7). We are unaware of any comparable analyses suggesting that k_f cannot be determined strictly from the fissure geometry. There are, however, several examples from the literature describing similitude laboratory experiments of naturally-ventilated buildings where the discharge coefficient, C_D, varies with the difference of density between the interior and exterior space – see e.g. Holford & Hunt (2001). Additionally there is theoretical evidence that effective permeabilities

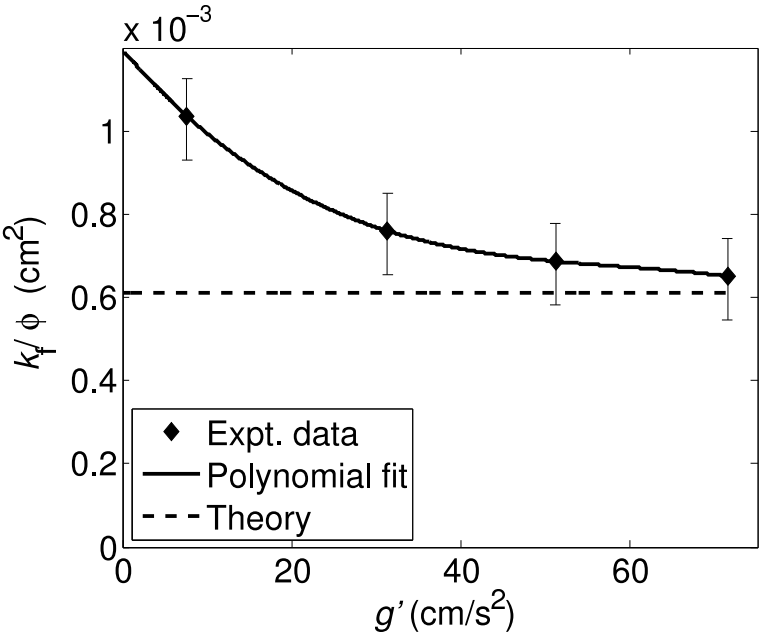

FIGURE 7. Variation of k_f/ϕ with $\bar{g}'$ as measured using the techniques summarized in §4. The theoretical prediction is based on (2.22) i.e. (5.10.3) of Bear (1972) and assumes well-developed outflow.

in porous media systems with more than one permeability may assume values that are influenced by buoyancy effects (Welty & Gelhar 1991, Bolster et al. 2011).

Figure 7 also includes a third-order polynomial best fit to the measured data, the dimensional equation of which reads

$$\frac{k_f}{\phi} = -2.11\times10^{-9}\,\frac{\mathrm{s}^6}{\mathrm{cm}}\,(\bar{g}')^3 + 3.73\times10^{-7}\,\mathrm{s}^4\,(\bar{g}')^2 - 2.35\times10^{-5}\,\mathrm{cm\,s}^2\,\bar{g}' + 1.20\times10^{-3}\,\mathrm{cm}^2\,. \tag{5.1}$$

From this empirical result and equations such as (2.18), which predict the reduced gravity of the dense lower layer as a function of F_0, ϕ, k, etc., one can estimate the particular value for k_f to be applied for a prescribed emptying filling box flow. This information is required in order to compare measured interface heights with analogue predictions, as we do in the following subsection.

5.2. *Comparison with theory*

Figure 8 displays a series of experimental images in which $\bar{g}_0' = 71.5\,\mathrm{cm}/s^2$, $Q_0 = 0.1\,\mathrm{mL/s}$, $b/H = 6.25 \times 10^{-2}$ and the normalized fissure cross-sectional area is decreased in equal steps from 9.35×10^{-2} to 2.34×10^{-2}. Consistent with analytical predictions, reducing $A/(\Lambda b)$ leads to a corresponding increase of interface height. The impact of the source reduced gravity is examined in figure 9 in which $\xi = h/H$ is shown as a function of $A/(\Lambda b)$ for three different values of $\bar{g}_0'$. Notably, $\bar{g}_0'$ exhibits only a small influence: in adjusting the source reduced gravity by a factor of more than five, the corresponding variation of ξ is typically less than the length of the canonical error bar indicated in panel c (c.f. Linden et al. 1990). Also shown in figure 9 are two sets of theoretical curves. In the case of the solid curves, we determine the solute dispersion coefficient, D, from the solution of (2.31). Conversely in the case of the dashed curves, mechanical dispersion is ignored and $D = D_{\mathrm{molecular}} = 2.5 \times 10^{-5}\,\mathrm{cm}^2/\mathrm{s}$ (Linden 1999). The dashed curves show the correct qualitative behavior, i.e. they predict the interface height to decrease with the fissure cross-sectional area (and, to a lesser extent, $\bar{g}_0'$). However, they significantly under-predict the magnitude of ξ. Much more satisfactory agreement between theory and experiment is realized in the case of the solid curves. Interestingly, the solid curves predict ξ to increase, albeit quite modestly, with $\bar{g}_0'$ for moderate and large $A/(\Lambda\, b)$. Analytically, this is due to the fact that by increasing $\bar{g}_0'$, both the source buoyancy flux, F_0, and D also increase. Because the Rayleigh number is proportional to F_0/D^2 (see equation 2.15), Ra decreases as the source reduced gravity increases from $12.5\,\mathrm{cm/s}^2$ to $42.0\,\mathrm{cm/s}^2$ to $71.5\,\mathrm{cm/s}^2$. (Counterbalancing this effect, note that the relative influence of the source volume flux, as measured by x_0/H, likewise decreases with increasing $\bar{g}_0'$.) We defer a more detailed investigation of this prediction to future investigations for several reasons: (i) the variation of ξ_{theory} with $\bar{g}_0'$ is, as noted above, minor whereas the trend of

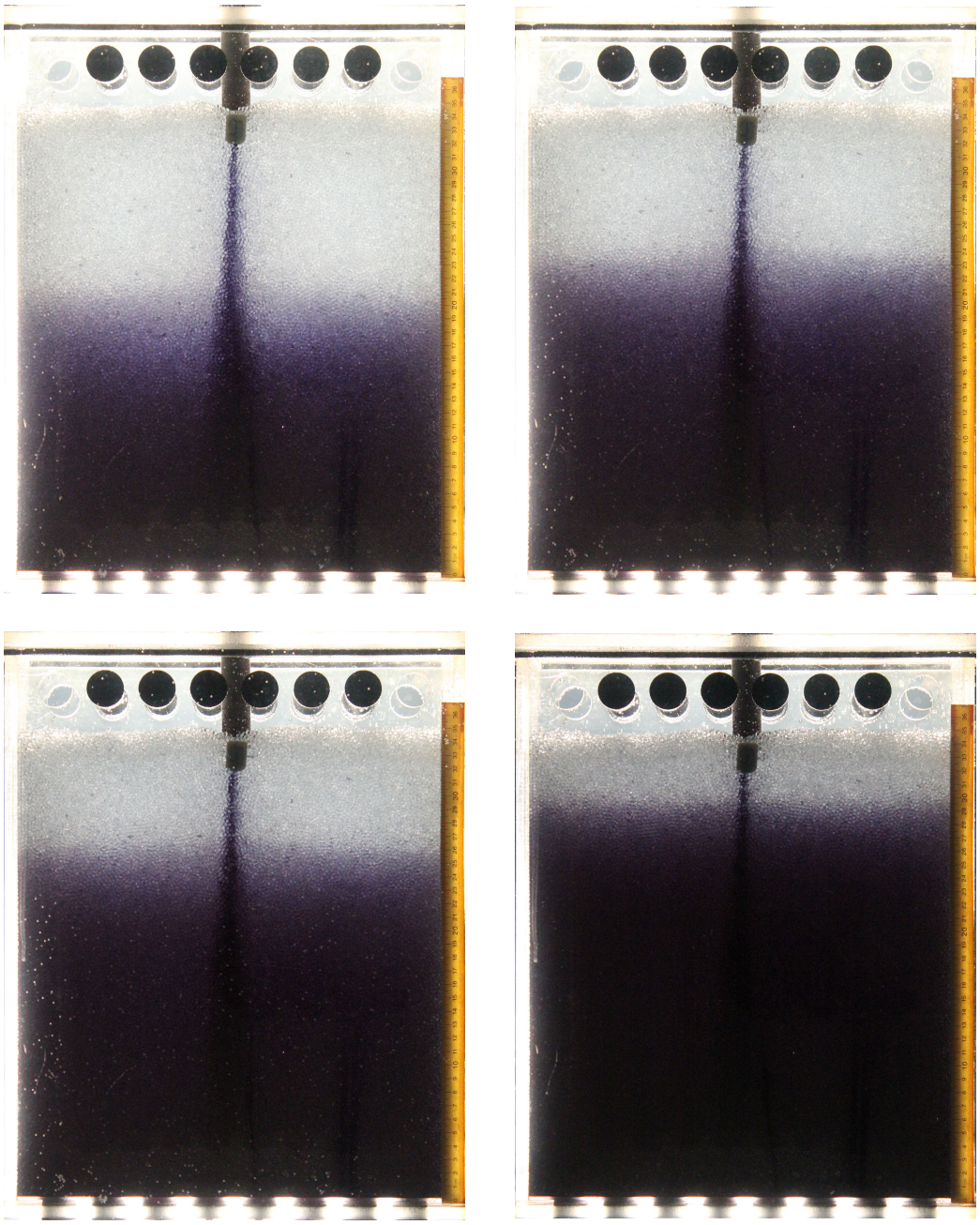

FIGURE 8. [color] The laboratory analogue of figure 1 b. As reported in text, all images share the same values for $\bar{g}_0'$, Q_0 and b/H, however, $A/(\Lambda b)$ decreases from 9.35×10^{-2} to 2.34×10^{-2} in increments of 2.34×10^{-2} in moving from the upper left to the upper right to the lower left to the lower right image. The yellow ruler that appears on the right-hand side in each panel is used in the measurement of h.

the experimental data is not definitive, and, (ii) the resolution may entail the introduction of an empirical parameter (c.f. Lai 1991) for which more sophisticated laboratory experiments, outside of the scope of the present inquiry, are necessary.

The open circles of figure 9 reappear as the horizontal dotted lines of figure 10, which shows the variation of the row-average false-color pixel intensity as a function of the normalized vertical coordinate, x/H. (The pixel intensity is here measured in arbitrary units; with reference to figure 8, recall that experimental images are cropped so that they exclude the vertical strip containing the descending plume). Figure 10 exploits a fact evident from figure 8, i.e. that the plume fluid is dyed so that pixel intensity may, in a false-color image, be used as an approximate surrogate for salt content. Instances where the intensity gradient seems to indicate the unstable scenario of heavy fluid overlying light fluid are due to spurious light reflections in the laboratory.

Of particular relevance in figure 10 is the inclusion of a pair of dashed lines derived from the numerical solution of (2.25); these indicate the upper and lower bounds associated with the interface given the value for h derived from the image processing routine summarized at the end of §4. Although the true interface thickness may be over- and under-estimated, respectively, in panels c and k/l, the general level of agreement between the prediction of (2.25) and the corresponding experimental profile is good. Most notably, (2.25) predicts ℓ to increase with $A/(\Lambda b)$ (i.e. to decrease with ξ), a trend that is clearly supported by the experimental data.

6. Conclusions

By combining the self-similar solution describing 2D-rectilinear or 2D-axisymmetric plume flow in a homogeneous porous medium with a draining law that prescribes the volume flux through a fissure as a function of the fissure area and the density of the

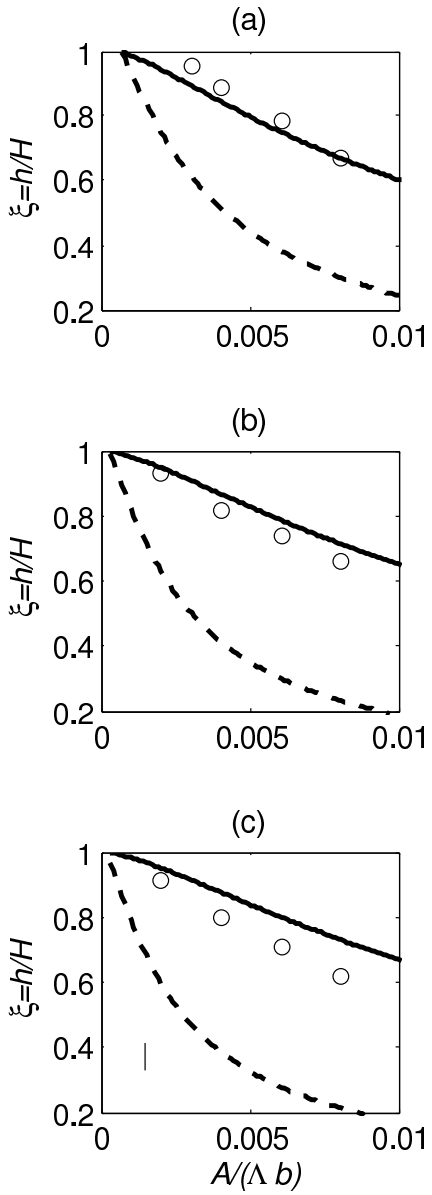

FIGURE 9. Non-dimensional interface height vs. fissure area. Analytical solutions are obtained by solving (2.19) using (5.1) supplemented by (2.18). The solid curves show the solution assuming D is given by (2.31) so that $\mathrm{Ra} = 7.36 \times 10^3$, $x_0/H = 0.0144$ ($\bar{g}_0' = 12.5\,\mathrm{cm/s^2}$); $\mathrm{Ra} = 4.88\times10^3$, $x_0/H = 2.06\times10^{-3}$ ($\bar{g}_0' = 42.0\,\mathrm{cm/s^2}$); and $\mathrm{Ra} = 4.39\times10^3$, $x_0/H = 8.76\times10^{-4}$ ($\bar{g}_0' = 71.5\,\mathrm{cm/s^2}$), respectively, in panels a, b and c. The dashed curves show the solution assuming diffusion by purely molecular processes. In all cases, $b/H = 6.25\times10^{-2}$. A representative error bar is indicated in panel c, whose experimental data points correspond to the laboratory images of figure 8.

draining fluid, it is possible to estimate the interface height, h, for the emptying filling box flow illustrated schematically in figure 1 b. Solutions are obtained by solving either a cubic or quadratic polynomial equation (i.e. equation 2.19 or 3.5, respectively) where, in either case, (i) the density of the draining fluid is assumed to match that of the plume at the position of the interface, and, (ii) the source volume flux, Q_0, is assumed to be finite. Critical to the success of our analysis, predictions from which are presented in figures 2, 3 and 5, is choosing the appropriate value for the solute dispersion coefficient, D. In the present context, it is assumed that transport by mechanical processes exceeds transport by molecular processes and that the appropriate characteristic velocity scale to apply in (2.10) corresponds to a transverse, not a longitudinal, speed. Thus the depth-average value of D is given by the solution of (2.31). Applying this result along with the information summarized in figure 7, which describes the flow resistance of the fissure as a function of the draining fluid density, one realizes positive agreement between theoretical predictions and analogue experimental measurements – see figure 9. In the latter circumstance, we restrict attention to the case of a line source but consider, as described in §4, multiple values for the source reduced gravity, $\bar{g}_0'$, and fissure area, A.

The analysis of §2 and §3 also provides a means of estimating the interface thickness, $2L$. Here the broadening influence of dispersion is counterbalanced against inflow into the plume yielding (2.25) and (3.10) for rectilinear and axisymmetric cases, respectively. A surprising, and as yet experimentally unverified, prediction associated with the latter equation is that it does not depend on the magnitude of D. This fact is related to the details of the self-similar solution given by (3.1) according to which the plume volume flux is predicted to vary linearly with D and the vertical coordinate x, but to be independent of the source buoyancy flux, F_0.

Fortunately, it is less cumbersome to verify, experimentally, the predictions of (2.25).

The associated comparison between theory and experiment is presented in figure 10 in which the row-average false-color pixel intensity associated with each of the measurements summarized in figure 9 is presented. On the basis of this comparison, we find there to be generally positive agreement between (2.25) and the analogue experimental data.

Relative to real geological or environmental flows, the present study is idealized in a number of respects. It considers a homogeneous porous medium only whereas, in actuality, vertical and even horizontal variations of the porosity, ϕ, and permeability, k, are not unlikely. Future research will consider these additional complications and will also seek to elucidate the time-dependent approach towards the steady state described, for example, by (2.13).

Acknowledgments

MRF's research is supported by NSERC (Discovery Grant and RTI programs) and Carbon Management Canada. DB would like to express thanks for financial support via NSF grant EAR-1113704. Financial support for MAR was generously provided, in part, by Dr. J. J. Leonard (Univ. of Alberta), who also added helpful insights over the duration of the research project. Fruitful conversations with Mr. Chunendra Sahu and Dr. Jerome A. Neufeld are also acknowledged, with thanks. Finally, the authors wish to acknowledge the Dept. of Mechanical Engineering Machine Shop at the Univ. of Alberta for technical support and also Dr. L. W. Sigurdson for providing laboratory space and infrastructure.

Appendix A. Line source – analytical details

The momentum equations (2.2) and (2.3) can be combined to eliminate the fluid pressure, i.e.

$$\frac{\nu}{k}\left(\frac{\partial u}{\partial y}-\frac{\partial v}{\partial x}\right)=\frac{g}{\rho_0}\frac{\partial \rho}{\partial y}\,. \tag{A 1}$$

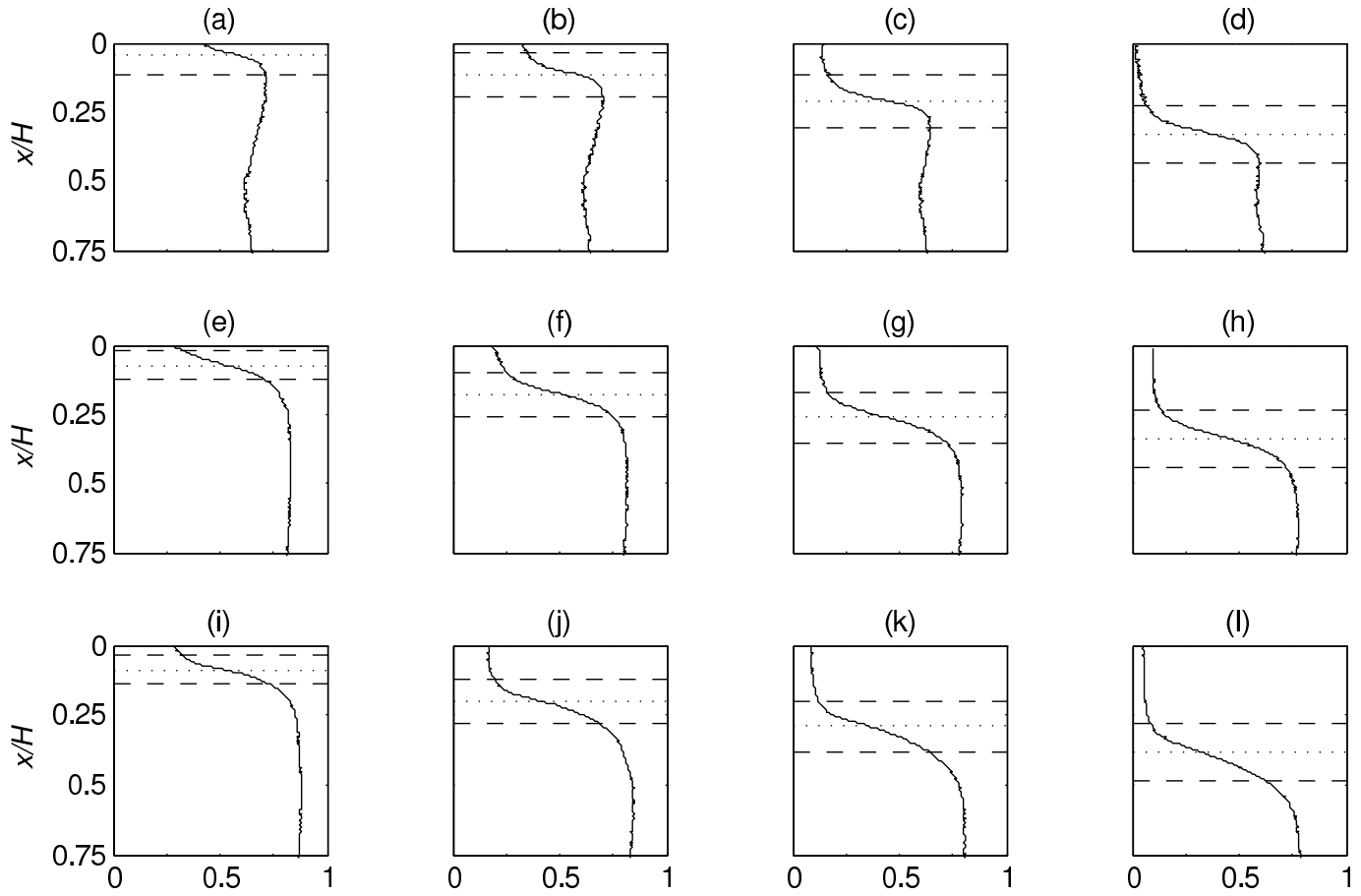

FIGURE 10. Row-average false-color pixel intensity (arbitrary units) vs. x/H. Panels a through d correspond, in sequential order, to the data points shown in figure 9 a. Likewise, panels e through h and i through l correspond, respectively, to the data points shown in figures 9 b and c. The dotted horizontal line indicates the experimental estimate for h (see figure 9). The dashed lines are based on the solution of (2.25) and show the associated analytical prediction for the interface thickness.

We now apply the boundary layer approximation (2.6) and introduce a stream-function ψ, defined so that

$$u = \frac{\partial \psi}{\partial y}\,, \qquad v = -\frac{\partial \psi}{\partial x}\,.$$

Equation (2.1) is then automatically satisfied whereas (A 1) and (2.4) become, respectively,

$$\frac{\partial^2 \psi}{\partial y^2} = \frac{g\beta k}{\nu}\frac{\partial S}{\partial y}\,, \tag{A 2}$$

and

$$\frac{\partial \psi}{\partial y}\frac{\partial S}{\partial x} - \frac{\partial \psi}{\partial x}\frac{\partial S}{\partial y} = D\phi\frac{\partial^2 S}{\partial y^2}\,. \tag{A 3}$$

We look for a self-similar solution to (A 2) and (A 3) of the form

$$\psi = Ax^{1/3} f(\eta)\,, \qquad S = \frac{B}{x^{1/3}} f'(\eta)\,, \tag{A 4}$$

where the prime indicates differentiation with respect to η, which is itself defined by

$$\eta = \frac{y}{x^{2/3}}\left[\frac{F_0 k}{(D\phi)^2 \Lambda \nu}\right]^{1/3}$$

(c.f. Wooding 1963, equation 20 c). The constants A and B are determined shortly.

Applying (A 4) in (A 2) allows us, after some algebra, to write B in terms of A, i.e.

$$B = \frac{A\nu}{g\beta k}\left[\frac{F_0 k}{(D\phi)^2 \Lambda \nu}\right]^{1/3}\,. \tag{A 5}$$

Meanwhile, applying (A 4) in (A 3) yields, after some further simplifications,

$$\left(\frac{D\phi F_0 k}{\Lambda \nu}\right)^{1/3} f''' + \tfrac{1}{3} A(ff')' = 0\,. \tag{A 6}$$

This result motivates us to define A as

$$A = \left(\frac{D\phi F_0 k}{\Lambda \nu}\right)^{1/3} \qquad \Rightarrow \qquad B = \frac{1}{g\beta}\left(\frac{F_0^2 \nu}{\Lambda^2 D\phi k}\right)^{1/3}\,, \tag{A 7}$$

where (A 5) has been applied. Integrating (A 6) recognizing that f' must vanish in the far-field where $S = 0$ yields

$$f' = \tfrac{1}{6}(c^2 - f^2)\,, \tag{A 8}$$

which has as its solution

$$f = c \tanh\left(\tfrac{1}{6} c\eta\right) . \tag{A 9}$$

The constant of integration, c, is determined by recalling that the buoyancy flux is independent of the vertical coordinate, x, provided the ambient is unstratified. In mathematical terms,

$$F_0 = \Lambda \int_{-\infty}^{\infty} u g' \, \mathrm{d}y \, , \tag{A 10}$$

where the integrand is evaluated at arbitrary x. Here the reduced gravity is defined by

$$g' = g\left(\frac{\rho - \rho_0}{\rho_0}\right) = g\beta S \, ,$$

the latter equality following from the (linear) equation of state (2.5). Applying this definition in (A 10) and recalling that $u = \partial\psi/\partial y$ yields, after some helpful cancellation of terms, $c = (9/2)^{1/3}$. With the solution (A 9) now unambiguously specified, both the plume volume flux and the velocity components u and v can be straightforwardly determined. In the former instance, note that

$$Q = \Lambda \int_{-\infty}^{\infty} u \, \mathrm{d}y = \Lambda [\psi]_{-\infty}^{\infty} \, , \tag{A 11}$$

where ψ is given in terms of f by (A 4 a). Using the previous results yields (2.8) from which (2.9) follows. In the latter instance, the vertical and horizontal velocities are given by (c.f. Wooding 1963 equations 20 a, b)

$$u = \left(\frac{9}{2x}\right)^{1/3} A C \operatorname{sech}^2\left(\frac{Cy}{x^{2/3}}\right) , \tag{A 12}$$

$$v = \left(\frac{9}{2}\right)^{1/3} A \left[\frac{2Cy}{3x^{4/3}} \operatorname{sech}^2\left(\frac{Cy}{x^{2/3}}\right) - \frac{1}{3x^{2/3}} \tanh\left(\frac{Cy}{x^{2/3}}\right)\right] , \tag{A 13}$$

respectively, where A is defined by (A 7) and

$$C = \frac{1}{6}\left(\frac{9}{2}\right)^{1/3} \left[\frac{F_0 k}{(D\phi)^2 \Lambda \nu}\right]^{1/3} . \tag{A 14}$$

Appendix B. Point source – analytical details

Whereas Appendix A considers a plume issuing from a line source, we now study the axisymmetric flow associated with a point source. Following Phillips (1991), it is expedient to introduce a Stokes stream-function, ψ_s, defined as

$$u_r = -\frac{1}{r}\frac{\partial \psi_s}{\partial x}\,, \qquad u = \frac{1}{r}\frac{\partial \psi_s}{\partial r}\,,$$

where r and u_r denote, respectively, the radial coordinate and velocity. Equations (A 2) and (A 3) are then expressed as

$$\frac{\partial}{\partial r}\left(\frac{1}{r}\frac{\partial \psi_s}{\partial r}\right) = \frac{g\beta k}{\nu}\frac{\partial S}{\partial r}\,, \tag{B 1}$$

and

$$\frac{1}{r}\frac{\partial \psi_s}{\partial r}\frac{\partial S}{\partial x} - \frac{1}{r}\frac{\partial \psi_s}{\partial x}\frac{\partial S}{\partial r} = \frac{D\phi}{r}\frac{\partial}{\partial r}\left(r\frac{\partial S}{\partial r}\right)\,, \tag{B 2}$$

respectively. Just as before, a self-similar solution is sought, now of the form

$$\psi_s = \check{A}x\mathcal{F}(\eta) \qquad S = \frac{\check{B}}{x}\mathcal{G}(\eta)\,, \tag{B 3}$$

where

$$\eta = \frac{r}{D\phi x}\cdot\sqrt{\frac{F_0 k}{2\pi\nu}}$$

(c.f. equations 7.5.24 and 7.5.25 of Phillips 1991). Applying these results in (B 1) yields

$$\mathcal{G} = \frac{1}{\eta}\mathcal{F}'\,, \tag{B 4}$$

provided $\check{B}$ is defined so that

$$\check{B} = \frac{F_0\check{A}}{2\pi g\beta(D\phi)^2}\,. \tag{B 5}$$

Meanwhile, (B 2) can be reduced to

$$-\mathcal{F}'(\mathcal{G}\eta)' - \mathcal{G}'(\mathcal{F} - \mathcal{F}'\eta) = \frac{D\phi}{\check{A}}(\mathcal{G}'\eta)'\,, \tag{B 6}$$

which motivates us to set $\breve{A} = D\phi$. Having done so, analytical solutions of (B 4) and (B 6) may be straightforwardly derived whereby

$$\psi_s = \frac{3D\phi x\eta^2}{8+\frac{3}{4}\eta^2}\,, \qquad S = \frac{3F_0}{8\pi g\beta D\phi x\left(1+\frac{3}{32}\eta^2\right)^2}\,. \tag{B 7}$$

Consistent with the discussion of Appendix A, the numerical values of the parameters in the previous expressions are determined by requiring that the buoyancy flux, defined as

$$F = 2\pi\int_0^\infty ug'\,r\mathrm{d}r\mathrm{d}\theta\,, \tag{B 8}$$

is independent of the vertical coordinate, i.e. $F = F_0$ for all x.

On the basis of the above calculations, it can be shown that

$$u_r = -\frac{3D\phi\eta^2}{r}\left[\frac{\frac{3}{4}\eta^2-8}{\left(\frac{3}{4}\eta^2+8\right)^2}\right]\,. \tag{B 9}$$

The far-field value of the radial speed therefore reads

$$|u_{r,ff}| = \frac{4D\phi}{r}\,. \tag{B 10}$$

The remarkable simplicity of (B 10) has the following important consequence (Phillips 1991): the rate of change of the plume volume flux with x must, by mass balance, satisfy

$$\frac{\mathrm{d}Q}{\mathrm{d}x} = \lim_{r\to\infty} 2\pi r|u_r|\,. \tag{B 11}$$

However, $r|u_{r,ff}| = 4D\phi$ so that the plume volume flux is given by the concise expression $Q = 8\pi D\phi x$. This formula can, of course, also be derived from $Q = 2\pi\int_0^\infty u\,r\mathrm{d}r$.

Appendix C. Experimental determination of k_f/ϕ – details

Equation (2.11) prescribes the rate at which fluid drains from the lower layer as a function of the fissure area, permeability, reduced gravity, etc. In the absence of replenishment (i.e. when the plume of figure 1 b is absent), the interface height will steadily

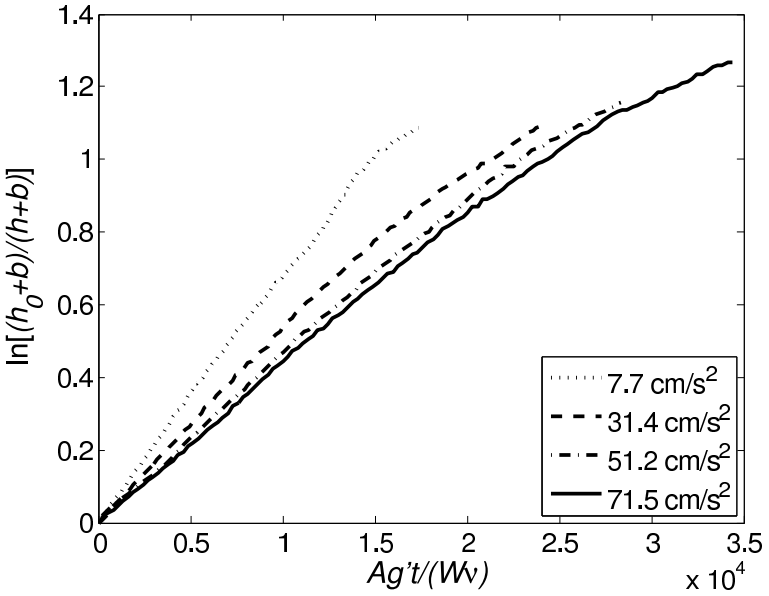

FIGURE 11. Interface height vs. time for four draining flow experiments where the legend entries indicate the values of $\bar{g}'$ and, in all cases, $A = 0.123\,\mathrm{cm}^2$. The slopes of the curves give the corresponding data points in figure 7.

decrease. By simple mass balance

$$-\Lambda W\phi\frac{\mathrm{d}h}{\mathrm{d}t} = \frac{Ak_f\bar{g}'}{\nu}\left(\frac{h+b}{b}\right). \tag{C 1}$$

Separating variables and integrating treating h_0 as the initial value for h, it can be shown that

$$\ln\left(\frac{h_0+b}{h+b}\right) = \frac{Ak_f\bar{g}'}{\nu b\Lambda W\phi}\cdot t\,. \tag{C 2}$$

According to (C 2) a plot of $\ln[(h_0+b)/(h+b)]$ vs. time, or its non-dimensional analogue $A\bar{g}'t/(W\nu)$, ought to yield a straight line from whose slope k_f/ϕ can be measured. Figure 11 shows such a plot from which the linear dependence of $\ln[(h_0+b)/(h+b)]$ and t can be confirmed, at least for $\ln[(h_0+b)/(h+b)] \lesssim 1$. Beyond this value, i.e. for $h \lesssim 10\,\mathrm{cm}$, the details of the draining flow may become more complicated than anticipated by (2.11).

Accordingly, when estimating k_f/ϕ from data such as are presented in figure 11, we restrict attention to the interval $0 \leq \ln[(h_0 + b)/(h + b)] \leq 1$.

REFERENCES

Acton, J. M., Huppert, H. E. & Worster, M. G. 2001 Two-dimensional viscous gravity currents flowing over a deep porous medium. *J. Fluid Mech.* **440**, 359–380.

Adalsteinsson, D., Camassa, R., Harenberg, S., Lin, Z., McLaughlin, R. M., Mertens, K., Reis, J., Schlieper, W. & White, B. L. 2011 Subsurface trapping of oil plumes in stratification: Laboratory investigations. *Geophysical Monograph Series* **195**, 257–262.

Baines, W. D. 1983 Direct measurement of volume flux of a plume. *J. Fluid Mech.* **132**, 247–256.

Baines, W. D. & Turner, J. S. 1969 Turbulent buoyant convection from a source in a confined region. *J. Fluid Mech.* **37**, 51–80.

Barrington, S., Choinière, D., Trigui, M. & Knight, W. 2003 Compost convective airflow under passive aeration. *Bioresource Technology* **86**(3), 259–266.

Bear, J. 1972 *Dynamics of Fluids in Porous Media*. Dover. 764 pp.

Bolster, D. T. & Linden, P. F. 2007 Contaminants in ventilated filling boxes. *J. Fluid Mech.* **591**, 97–116.

Bolster, D. T., Neuweiler, I., Dentz, M. & Carrera, J. 2011 The impact of buoyancy on front spreading in heterogeneous porous media in two-phase immiscible flow. *Water Resources Res.* **47**(2).

Bower, D. J., Caulfield, C. P., Fitzgerald, S. D. & Woods, A. W. 2008 Transient ventilation dynamics following a change in strength of a point source of heat. *J. Fluid Mech.* **614**, 15–37.

Drysdale, D. 2011 *An Introduction to Fire Dynamics*. Wiley. com.

Fetter, C. W. 1993 *Contaminant Hydrogeology*. McMillan, New York. 458 pp.

Flynn, M. R. & Caulfield, C. P. 2006 Natural ventilation in interconnected chambers. *J. Fluid Mech.* **564**, 139–158.

Freeze, R. A. & Cherry, J. A. 1979 *Groundwater*. Prentice Hall, Englewood Cliffs, NJ. 604 pp.

Germeles, A. E. 1975 Forced plumes and mixing of liquids in tanks. *J. Fluid Mech.* **71**, 601–623.

Happel, J. & Brenner, H. 1991 *Low Reynolds Number Hydrodynamics: With Special Applications to Particulate Media*, volume 2nd. Kluwer Academic.

Holford, J. M. & Hunt, G. R. 2001 The dependence of the discharge coefficient on denity contrast – Experimental measurements. In *Proc. 14th Australian Fluid Mechanics Conf., Adelaide Univ.* , , 123–126.

Houseworth, J. E. Longitudinal dispersion in nonuniform isotropic porous media. Technical Report KH-R-45, W. M. Keck Laboratory of Hydraulics and Water Resources, Division of Engineering and Applied Science, California Inst. of Tech., 1984.

Joseph, D. D., Nield, D. A. & Papanicolaou, G. 1982 Nonlinear equation governing flow in a saturated porous medium. *Water Resources Res.* **18**, 1049–1052.

Kaye, N. B., Flynn, M. R., Cook, M. J. & Ji, Y. 2010 The role of diffusion on the interface thickness in a ventilated filling box. *J. Fluid Mech.* **652**, 195–205.

Kaye, N. B. & Hunt, G. R. 2004 Time-dependent flows in an emptying filling box. *J. Fluid Mech.* **520**, 135–156.

Kaye, N. B. & Hunt, G. R. 2007 Smoke filling time for a room due to a small fire: The effect of ceiling height to floor width aspect ratio. *Fire Safety Journal* **42**(5), 329–339.

Killworth, P. D. 1983 Deep convection in the World ocean. *Reviews of Geophysics* **21**(1), 1–26.

Kuo, E. Y. & Ritchie, A. I. M. 1999 The impact of convection on the overall oxidation rate in sulfidic waste rock dumps. *Proceedings Mining and the Environment II 1999* pages 211–220.

Lai, F. C. 1991 Non-Darcy natural convection from a line source of heat in a saturated porous medium. *Int. Comm. Heat Mass Transfer* **18**, 445–457.

Linden, P. F. 1999 The fluid mechanics of natural ventilation. *Ann. Rev. Fluid Mech.* **31**, 201–238.

Linden, P. F., Lane-Serff, G. F. & Smeed, D. A. 1990 Emptying filling boxes: the fluid mechanics of natural ventilation. *J. Fluid Mech.* **212**, 309–335.

McDougall, T. J. 1978 Bubble plumes in stratified environments. *J. Fluid Mech* **85**(4), 655–672.

Morton, B. R., Taylor, G. I. & Turner, J. S. 1956 Turbulent gravitational convection from maintained and instantaneous sources. *Proc. Roy. Soc. A* **234**, 1–23.

Nabi, S. & Flynn, M. R. 2014 Influence of geometric parameters on the eventual buoyancy stratification that develops due to architectural exchange flow. *Building and Environment* **71**, 33–46.

National-Research-Council, 2012 *Alternatives for Managing the Nation's Complex Contaminated Groundwater Sites*. Committee on Future Options for Management in the Nation's Subsurface Remediation Effort and Water Science and Technology Board (WSTB) and Division on Earth and Life Studies (DELS); The National Academies Press.

Neufeld, J. A., Vella, D. & Huppert, H. E. 2009 The effect of a fissure on storage in a porous medium. *J. Fluid Mech.* **639**, 239–259.

Neufeld, J. A., Vella, D., Huppert, H. E. & Lister, J. R. 2011 Leakage from gravity currents in a porous medium. Part 1. A localized sink. *J. Fluid Mech.* **666**, 391–413.

Nield, D. A. & Kuznetsov, A. V. 2013 An historical and topical note on convection in porous media. *Journal of Heat Transfer* **135**, 061201.

Nordbotten, J. M., Celia, M. & Bachu, S. 2004 Analytical solutions for leakage rates through abandoned wells. *Water Resources Res.* **40**(4), W04204.

Phillips, O. M. 1991 *Flow and Reactions in Permeable Rocks*. Cambridge University Press, Cambridge, 1st edition. 285 pp.

Pritchard, D. & Hogg, A. J. 2002 Draining viscous gravity currents in a vertical fracture. *J. Fluid Mech.* **459**, 207–216.

Riaz, A., Hesse, M., Tchelepi, H. A. & Orr, F. M. 2006 Onset of convection in a gravitationally unstable diffusive boundary layer in porous media. *J. Fluid Mech.* **548**, 87–111.

Roes, M. A. Buoyancy-driven convection in a ventilated porous medium. Master's thesis, Univ. of Alberta, 2014.

Rumpf, H. & Gupte, A. R. 1971 Einflüsse der porosität und Korngrössenverteilung im Widerstandsgesetz der Poreströmung. *Chem. Ing. Tech.* **43**, 367–375.

Speer, K. G. & Rona, P. A. 1989 A model of an Atlantic and Pacific hydrothermal plume. *J. Geophysical Research: Oceans (1978–2012)* **94**(C5), 6213–6220.

Szulczewski, M. L., Hesse, M. A. & Juanes, R. 2013 Carbon dioxide dissolution in structural and stratigraphic traps. *J. Fluid Mech.* **736**, 287–315.

Turcotte, D. L. & Schubert, G. 2014 *Geodynamics*. Cambridge University Press, Cambridge, England, 3rd edition. 636 pp.

Turner, J. S. & Campbell, I. H. 1986 Convection and mixing in magma chambers. *Earth-Science Reviews* **23**(4), 255–352.

Welty, C. & Gelhar, L. W. 1991 Stochastic analysis of the effects of fluid density and viscosity variability on macrodispersion in heterogeneous porous media. *Water Resources Research* **27**(8), 2061–2075.

Wong, A. B. D. & Griffiths, R. W. 2001 Two-basin filling boxes. *J. Geophys. Res.-Oceans* **106**, 26,929–26,941.

Wooding, R. A. 1963 Convection in a saturated porous medium at large Rayleigh number or Péclét number. *J. Fluid Mech.* **15**, 527–544.

Woods, A. W. 1988 The fluid dynamics and thermodynamics of eruption columns. *Bulletin of Volcanology* **50**(3), 169–193.

Woods, A. W. 2010 Turbulent plumes in nature. *Annu. Rev. Fluid Mech.* **42**, 391–412.

Wüest, A., Brooks, N. H. & Imboden, D. M. 1992 Bubble plume modeling for lake restoration. *Water Resources Res.* **28**, 3235–3250.